01 Mar 2019

Seismicity Enhances Macrodispersion in Finite Porous and Fractured Domains: A Pore-Scale Perspective

Lizhi Zheng

Lichun Wang

Wen Deng
Missouri University of Science and Technology, wendeng@mst.edu

Recommended Citation

L. Zheng et al., "Seismicity Enhances Macrodispersion in Finite Porous and Fractured Domains: A Pore-Scale Perspective," *Journal of Geophysical Research: Solid Earth*, vol. 124, no. 3, pp. 2844-2857, Blackwell Publishing Ltd, Mar 2019.
The definitive version is available at https://doi.org/10.1029/2018JB016921

JGR Solid Earth

RESEARCH ARTICLE
10.1029/2018JB016921

Key Points:
- The oscillating flow field in pore-scale porous and fractured media is simulated by applying different seismic forces
- Two-hundred twenty simulated breakthrough curves demonstrate maximized macrodispersion when oscillating flow field *resonates* with finite domain
- The degree of enhancement in macrodispersion increases exponentially with the amplitude of the seismic force

Supporting Information:
- Supporting Information S1
- Movie S1
- Movie S2
- Movie S3
- Movie S4
- Movie S5
- Movie S6
- Movie S7
- Movie S8

Correspondence to:
L. Wang,
wanglichun@tju.edu.cn

Citation:
Zheng, L., Wang, L., & Deng, W. (2019). Seismicity enhances macrodispersion in finite porous and fractured domains: A pore-scale perspective. *Journal of Geophysical Research: Solid Earth*, *124*. https://doi.org/10.1029/2018JB016921

Received 22 OCT 2018
Accepted 15 FEB 2019
Accepted article online 20 FEB 2019

Seismicity Enhances Macrodispersion in Finite Porous and Fractured Domains: A Pore-Scale Perspective

Lizhi Zheng[1], Lichun Wang[2], and Wen Deng[3]

[1]Department of Geological Sciences, The University of Texas at Austin, Austin, TX, USA, [2]Institute of Surface-Earth System Science, Tianjin University, Tianjin, China, [3]Department of Civil, Architectural and Environmental Engineering, Missouri University of Science and Technology, Rolla, MO, USA

Abstract Understanding the effects of oscillating flow field induced by seismicity on the transport process is vital for predicting the fate and transport of solute in many dynamic environments. However, there is prominent discrepancy in arguing with the response of dispersion to the oscillating flow field (i.e., the longitudinal dispersion coefficient would decrease, increase, or maintain unchanged). To unravel the underpinning physics about this controversial response, we simulated two-hundred twenty pore-scale numerical experiments for the seismicity-induced oscillating flow field and associated solute transport in the idealized finite porous (i.e., fluidic plate) and fractured (i.e., parallel plates) domains. The numerically obtained breakthrough curves were fitted to the macroscopic advection-dispersion equation to retrieve the mean velocity and apparent macrodispersion coefficient (D_L). We found that D_L increases to its maxima when the oscillating flow field *resonates* with the finite systems, that is, the period (T) of the oscillating flow field or the seismic wave approaches the pore volume (τ) of a finite domain. The *resonant* effects diminish and D_L barely changes when T is much larger or smaller than τ. Moreover, the degree of enhancement in D_L increases exponentially with the amplitude of the seismic force. Fundamental understanding of the response of macrodispersion to the oscillating flow field adds value in predicting the fate of solute in transient flow systems via the advection-dispersion equation.

Plain Language Summary The fate and transport of solute mainly depend on the advection and dispersion processes that tie to the flow field. The challenge of quantifying the flow field lies in the complexity of characterizing heterogeneous geological media. Moreover, the flow field can be oscillating periodically in some geological settings. When present, the oscillating flow field can substantially alter the solute transport process. However, many researchers hold controversial arguments about the effects of the oscillating flow field on the macroscopic dispersion process (i.e., macrodispersion). In this study, we unravel the effects of the seismicity-induced oscillating flow field on macrodispersion in finite domains. Two-hundred twenty pore-scale numerical flow and transport experiments have been done through the idealized finite porous and fractured domains. We find that the macrodispersion coefficient maximizes when the period of the oscillating flow field approaches the flushing time of a finite domain. The enhancement of macrodispersion increases exponentially with the amplitude of the seismic wave and oscillating flow field. Our study quantitatively reveals the enhanced macrodispersion feature at a mechanistic level that might shed light on predicting solute transport in many other transient flowing systems.

1. Introduction

A better understanding of spreading and mixing of solute in geological media is critical for predicting the fate of solute and contaminants in many geological systems (Dentz et al., 2011). Essentially, the dispersion process dictates the rate of spreading and mixing (Fischer et al., 1979). Therefore, there are increasing numbers of literatures investigating the dispersion problem. For example, many researchers revealed that the spatial variability of the velocity field induced by the material heterogeneity can enhance macroscopic dispersion (Cirpka et al., 2015; Dentz, le Borgne, et al., 2011). This has been also demonstrated by a fact that the dispersion coefficient is a scale-dependent property for porous and fractured media (Gelhar & Axness, 1983). Indeed, the influence of spatial heterogeneity on flow often leads to non-Fickian transport where the early arrival and long tailing of breakthrough curves (BTCs) are expected to occur (Le Borgne et al., 2008; Wang & Cardenas, 2014). Therefore, all factors that alter the spatial heterogeneity of a geological media might cause non-Fickian transport (Kang et al., 2016) and enhance the macrodispersion process.

Furthermore, in many natural environments, temporal fluctuation of the velocity field exists in geological media and plays a significant role in affecting transport process. This temporal fluctuation can be induced by the boundary conditions of fluctuating water levels caused by, for example, hydrological cycle, plants evapotranspiration, and Earth tides that oscillate daily, seasonally, and even annually (Boutt & Fleming, 2009; Deon et al., 2017). Or, the temporal fluctuation can be caused by the imposed body force caused by, for example, earthquakes, constructions, and traffic noise (Manga et al., 2012). Recently, fluid injection has been also proposed to cause seismicity at the regional scale (Elsworth et al., 2016; Weingarten et al., 2015). A better understanding on how the temporal velocity fluctuation affects transport is important to improve the theory of complex transport process in geological media. Our study focused on solute transport that is affected by the seismicity-induced oscillating flow.

To address and quantify the dispersion process induced by the temporally fluctuating flow, studies mainly relied on theoretical analysis (Dentz et al., 2011; Dentz & Carrera, 2003, 2005; Rehfeldt & Gelhar, 1992; Zhang & Neuman, 1996), and a few researches resorted to the physical (Zhang et al., 2009) and numerical (Dreuzy et al., 2012; Pool et al., 2016) experiments. In any case, all studies confirmed that the transverse dispersion coefficient will be enhanced to some extent due to the temporal velocity fluctuation (Cirpka et al., 2015; Cirpka & Attinger, 2003). However, there is a large discrepancy with respect to the longitudinal dispersion coefficient (D_L) under the influence of temporal velocity fluctuation.

Over the last four decades, many researchers have suggested that D_L increases under the oscillating flow for idealized cases (Chatwin, 1975) and natural environments (Dentz & Carrera, 2005). However, some recent studies found, D_L can decrease (Zhang & Neuman, 1996), or fairly maintain constant (Dentz, Carrera, & De Dreuzy, 2011; Dreuzy et al., 2012) when the oscillating flow field was present, or even fluctuated over time in response to the oscillating flow (Elfeki et al., 2007). The mechanisms of these controversial arguments about the effects of the oscillating flow on D_L are not quite clear. Previous study indicated that the truncation of certain terms in the stochastic perturbation method for theoretically deriving D_L can yield quite opposite results, that is, the resulting effect switches from increased D_L to barely changed D_L (Dentz, Carrera, & De Dreuzy, 2011). However, more work is needed to elucidate the underpinning mechanisms of how the oscillating flow field affects D_L. That is, how to quantitatively connect the frequency and amplitude of the oscillating flow with D_L. This study addresses these questions based on hundreds of pore-scale simulations.

Unlike previous studies that focused on infinite systems at the continuum scale (Dreuzy et al., 2012), our study tries to address the above-mentioned controversial problem about the effects of the oscillating flow field on D_L in a finite geological domain at the pore scale (millimeter scale); the domain studied here has a fixed intrinsic timescale (i.e., pore volume or residence time). This is because many natural environments are having a finite domain, or at least, the magnitude of timescale of a system is in the same order of magnitude to the period of the oscillating flow field. For example, the hyporheic zones that link surface water and groundwater in the Mississippi River network have residence time distributions ranging from below 1 hr to above 1 year (Kiel & Bayani Cardenas, 2014), and the external force, that is, surface water level fluctuates daily and seasonally (Michael et al., 2005). This suggests that the period of the fluctuating velocity in the hyporheic zones is comparable and relevant to their residence timescale. Moreover, the coastal intertidal zone is another great finite domain example that is spatially limited by the magnitude and period of ocean tides (Befus et al., 2013). Given a wide presence of finite flowing domains, understanding solute transport in such a finite domain has been however underappreciated, especially considering the oscillating flow field; this motivates our study to unravel the complexity of transport caused by the transient flow field. The pore-scale simulations served our purpose for fundamentally explaining the effects of the oscillating flow fields on macrodispersion.

For a finite flowing domain, we hypothesize that D_L increases only when the intrinsic timescale (i.e., pore volume τ) of a finite system is identical to or at the same order of magnitude of the period (T) of the temporally oscillating flow field. We denote these phenomena as *resonant* effect when $\tau \approx T$ in this study. Here τ is defined as flushing time or pore volume at steady state; τ is the ratio of the volume of void space of the finite domain to the time-averaged flushing discharge. Moreover, we hypothesize that when T is much greater or smaller than τ, the resonant effects diminish and D_L barely changes in response to the oscillating flow field. To attest our hypotheses, we resorted to hundreds of pore-scale numerical transport experiments in porous

and fractured media by varying T while keeping τ constant. The results of reliable numerical experiments supported our hypotheses as further discussed below.

2. Methodology

The exploratory pore-scale numerical transport experiments were conducted through two-dimensional (2D) idealized pores and a fracture (Figure 1); the 2D cases are sufficient to attest our hypotheses and to avoid unnecessary computational burden that might be encountered in a three-dimensional domain. We first solved the flow field governed by the Navier-Stokes equation (NSE) via COMSOL Multiphysics for an idealized homogeneous porous media (i.e., a fluidic plate with porosity = 0.29 in Figure 1a) and via the analytical solution for an idealized fracture (i.e., a parallel-plate model in Figure 1b). For simplicity, the transient flow field was subject to a body force induced by the imposed seismic wave (Deng & Cardenas, 2013). To mitigate numerical dispersion especially when the flow field oscillated to a certain degree, we resorted to the particle tracking random walk (PTRW) to model a conservative solute transport process by MatLab. The details of solving the flow field and solute transport are further elaborated below.

2.1. Oscillating Flow Field in Homogeneous Porous Media and Fractures

Fluid flow through a 2D porous and fractured media is essentially governed by the NSE (Bear, 1972). The incompressible and isothermal NSE considering seismicity at transient state is described by (Deng & Cardenas, 2013)

$$\begin{cases} \rho\dfrac{\partial \boldsymbol{u}}{\partial t} + \rho\nabla\cdot(\boldsymbol{u}\boldsymbol{u}) = -\nabla P + \mu\left(\nabla\boldsymbol{u} + \nabla\boldsymbol{u}^{\mathrm{T}}\right) + F \\ \nabla\cdot\boldsymbol{u} = 0 \end{cases} \tag{1}$$

where ρ (1,000 kg/m^3) is fluid density, $\boldsymbol{u}$ is velocity vector, μ (0.001 Pa-s) is dynamic fluid viscosity, P is total pressure, t is time, and F is an oscillating body force induced by the seismic wave that follows a sinusoidal function (Beresnev, 2006)

$$F = -\rho A \sin(2\pi f t) \tag{2}$$

where A represents the acceleration amplitude and f is the frequency (i.e., the reciprocal of period T) of the seismic wave. In this study, f and T refer to the timescale of the oscillating flow field.

For a seismic wave, the observed f varies largely from low ~1×10^{-3} Hz to high ~1×10^{2} Hz magnitudes in geological systems induced by earthquake or episodic tremor and slip (Beresnev, 2006; Deng & Cardenas, 2013; Ito & Obara, 2006). Additionally, the undetected f might be much lower than the reported value due to seismic attenuation (Pride et al., 2004). Considering the wide range of f, we turned to the seismic wave rather than other factors (e.g., ocean tides (Chambers et al., 2002)) to generate the oscillating flow field in this study. The possible range of f used in this study was set to be flexible (1×10^{-5}–1×10^{2} Hz). This is exemplified by the different colored lines (i.e., represent various T) in Figure 2. More imposed seismic waves with different f are not shown here. Besides the effects induced by f or T (= $1/f$), we altered the amplitude A to further examine the effects of a seismic wave on the macrodispersion process (Figure 2). In short, we investigated the effects of dimensionless amplitude ($\rho A/\nabla P$) and dimensionless period (T/τ) on the transport process.

For solving the flow field in a finite porous media, we imposed a fixed pressure (i.e., pressure gradient ∇P = 5,000 Pa/m) at the inlet and outlet that drove flow in the longitudinal (i.e., x) direction (Figure 1a). This resulted in a constant τ. The top and bottom sides were set as no flux (i.e., no-slip) boundaries. Moreover, we incrementally increased T and A in equation (2) to generate oscillating flow fields accordingly. T and A were nondimensionalized using the fixed ∇P and τ as exemplified in Figure 2. Specifically, $\rho A/\nabla P$ increased from 0.2 to 1.6, and T/τ spanned from 0.0066 to 6.67. In total, we implemented $8 \times 8 \times 2$ numerical experiments for both flow and transport processes within the finite fluidic plate.

For the finite parallel plates, the inlet and outlet were also specified as a fixed pressure boundary condition (i.e., pressure gradient ∇P = 10 Pa/m) that drove flow in the x direction (Figure 1c). No slip boundary was

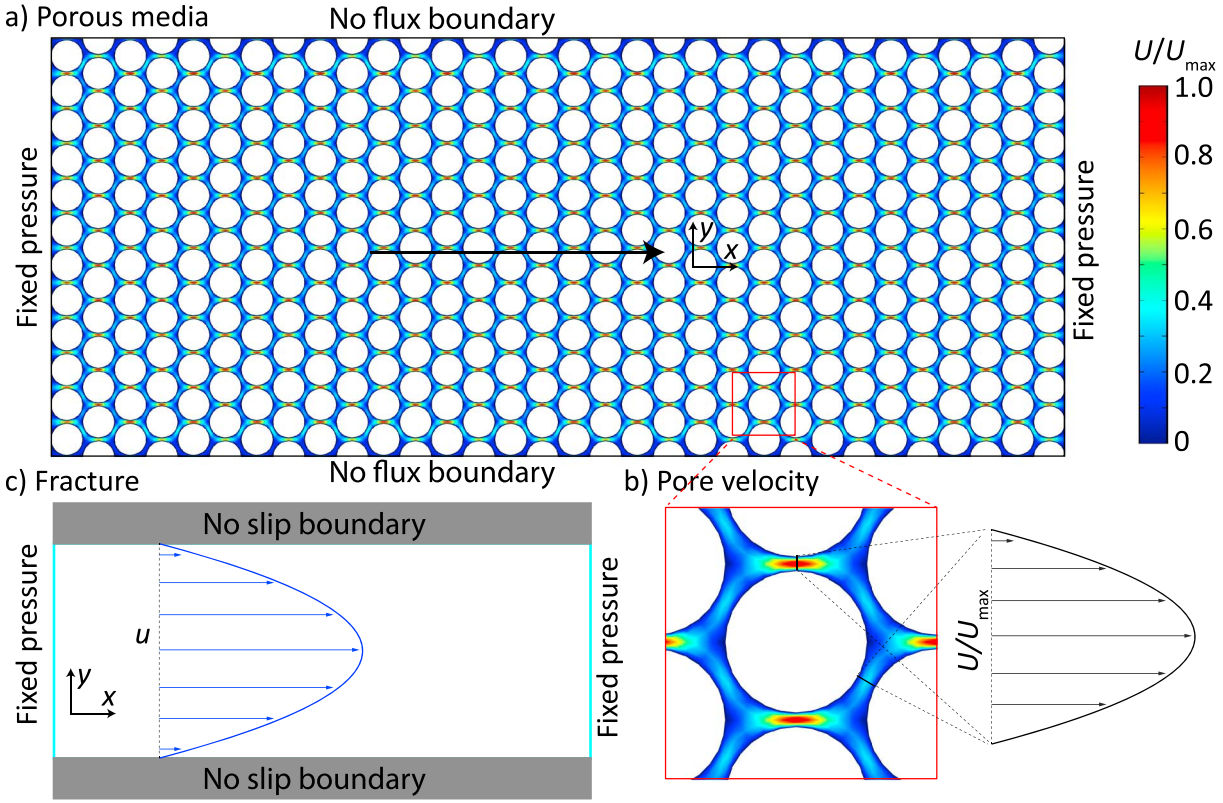

Figure 1. The schematic diagram for demonstrating the snapshot of the oscillating velocity field in a fluidic plate (a and b) and in a parallel plates (c). (a) The fluidic plate consists of connected pore bodies by pore throat surrounded by the solid grains (i.e., the hollow circles). The colored velocity field is driven by the pressure gradient with fluid flowing in the x direction as indicated by the black arrow. The top and bottom surfaces are no flux boundaries. (b) The detailed velocity for a representative block within the fluidic plate, where the local velocity fairly follows the parabolic shape. (c) The velocity profile across the parallel plates strictly follows a parabolic shape. The pressure gradient drives fluid flowing in the x direction. No slip boundary is specified for the top and bottom sides surrounded by the gray matrix.

applied to the bottom and top surfaces. The analytical solution to the flow field governed by the NSE with the imposed seismic wave can be described as (Fischer et al., 1979; Wang et al., 2012)

$$u(y) = \frac{b^2}{8\mu}\left(1-\frac{4y^2}{b^2}\right)(\nabla P + \rho A \sin(2\pi f t)) \quad (3)$$

where b is the fracture aperture and y represents the transverse direction that is perpendicular to the x direction (Figure 1c). The parabolic profile of u was homogeneous in the longitudinal direction for a given A and f, where $\rho A/\nabla P$ increased from 0.5 to 10, and T/τ spanned from 0.0083 to 83.3; this was achieved by increasing A and f with constant ∇P and τ. In total, we have done 6×26 numerical experiments for the transport process within the parallel plates. The wider range of $\rho A/\nabla P$ and T/τ was used to further attest the resonant effects on macrodispersion. The details of τ for the finite fluidic plate and parallel plates are further discussed below.

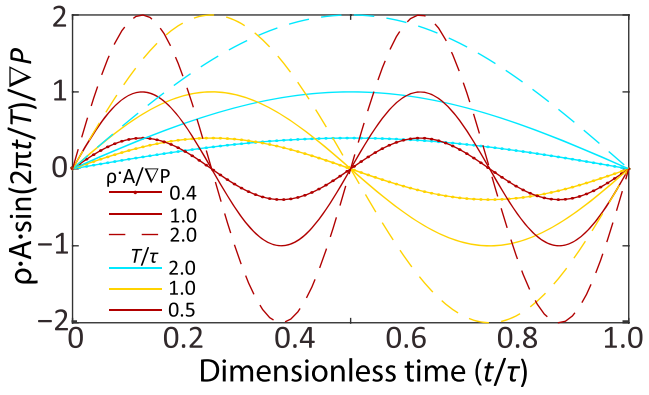

Figure 2. The explanatory seismic body forces with a varying degree of dimensionless period T/τ and dimensionless amplitude $\rho A/\nabla P$, where T and A are period and amplitude of a seismic wave, τ is pore volume (i.e., volume/discharge) of a finite system, ρ is fluid density, t is time, ∇P is pressure gradient that drives fluid flowing in the longitudinal direction as demonstrated in Figure 1, and sin() represents the sinusoidal function.

2.2. The Fixed Pore Volume (τ) of Finite Porous and Fractured Media

2.2.1. The Fluidic Plate Representing Porous Media

We designed a fluidic plate (Figure 1a) that has width = 6.6×10^{-4} m, length = 1.6×10^{-3} m, depth = 1 unit, the individual radius of

grain = 2.5×10^{-5} m, area of void space = 3.08×10^{-7} m^2, and porosity = area of void space/total area = 0.29. Given an imposed ∇P = 5,000 Pa/m without seismic force ($A = 0$ and $f = 0$ in equation (2)), the resultant discharge = 2.04×10^{-9} m^3/s. Therefore, τ = volume/discharge = 151.3 s.

2.2.2. The Parallel Plates Representing Fracture

The parallel plates have an aperture $b = 5 \times 10^{-4}$ m, length = 0.025 m, and volume = 1.25×10^{-5} m^3 assuming one unit width. The imposed $\nabla P = 10$ Pa/m resulted in discharge = 1.04×10^{-7} m^3/s without considering seismic force ($A = 0$ and $f = 0$ in equation (2)). Thus, τ = volume/discharge = 120 s for the microfracture studied here.

2.3. PTRW for Simulating Solute Transport

Given that the finite porous and fractured systems all have a constant τ for the given ∇P at laminar flow regime, hereafter, we analyzed the effects of dimensionless period T/τ on macrodispersion by fixing τ but varying T. The resultant oscillating fields subjected to the seismic waves with different A and f were used to simulate the solute transport process.

The 2D numerical transport experiments were implemented via the PTRW. Generally, the PTRW keeps track of individual particles' location considering their advective and diffusive jumps (James et al., 2005; Wang & Cardenas, 2015)

$$\mathbf{x}^{n+1} = \mathbf{x}^n + \mathbf{u}(\mathbf{x}^n, n\Delta t)\Delta t + N(0,1)\sqrt{2\mathrm{D_m}\Delta t} \tag{4}$$

where $\boldsymbol{x}\,[x, y]$ denotes the spatial location of a given particle, n is current time step, $n + 1$ is future time step, $\mathbf{u}$ is velocity vector, Δt is time step size, $N(0, 1)$ is an independent number picked from the standard normal distribution with mean value = 0 and variance = 1, and D_m is molecular diffusion coefficient (2.03×10^{-9} m^2/s).

The PTRW was implemented through MatLab. The main difference in implementing transport simulations in porous and fractured media lied in the treatment of particles' reflection; that is, the reflection by the solid grain (i.e., the circle) within a porous media is different from that by the top and bottom surfaces of a fracture. Here we provided the schematic diagrams (Figure 3) and the mathematic expressions (Appendices A1 and A2.) on handling particles' reflection by the solid surfaces. In any case, the reflection principle was employed when a particle hit the solid surfaces without energy loss to satisfy no-flux boundary condition (James & Chrysikopoulos, 2000).

We released 5×10^3 particles for both porous and fractured media. Numerical results were insensitive to the further increase of number of particles (results are not shown here). The PTRW was implemented with an adaptive time step. The time step was updated every time step and was determined by min(T/20, scale^2/[20 · D_m], scale^2/[10 · velocity]), where min() represents the minimum function, scale = radius of grain (Figure 1) for the fluidic plate, and scale = aperture for the parallel plates. This ensured a balance between computational efficiency and simulation accuracy (Detwiler et al., 2002; Wang & Cardenas, 2015).

The ratio of cumulative particles arriving at the outbound to the total number of particles constitutes the BTCs. The macrodispersion coefficient (D_L) was obtained by fitting the classical macroscopic advection-dispersion equation to the BTCs from PTRW solutions (Wang & Cardenas, 2017).

2.4. The Apparent Dispersion Coefficient for Describing Macrodispersion

Generally, there are two broadly applied methods for quantifying the dispersion process: (1) fitting the macroscopic advection-dispersion equation to the measured BTCs to obtain the apparent dispersion coefficient (Gelhar et al., 1992); (2) quantifying the actual spreading of solute based on the first and second moments of a solute plume via the effective or ensemble dispersion coefficient (Dentz & Carrera, 2003, 2005). In this study, we relied on the first method to estimate the apparent D_L because (a) we attempted to reproducing the numerically measured BTCs, and (b) the effective or ensemble D_L determined by the second method changes over time (Wang & Cardenas, 2015). Indeed, the first method was more convenient to analyze constant D_L for different cases than the second method, because the latter is supposed to produce varying D_Ls in response to the oscillating velocity fields.

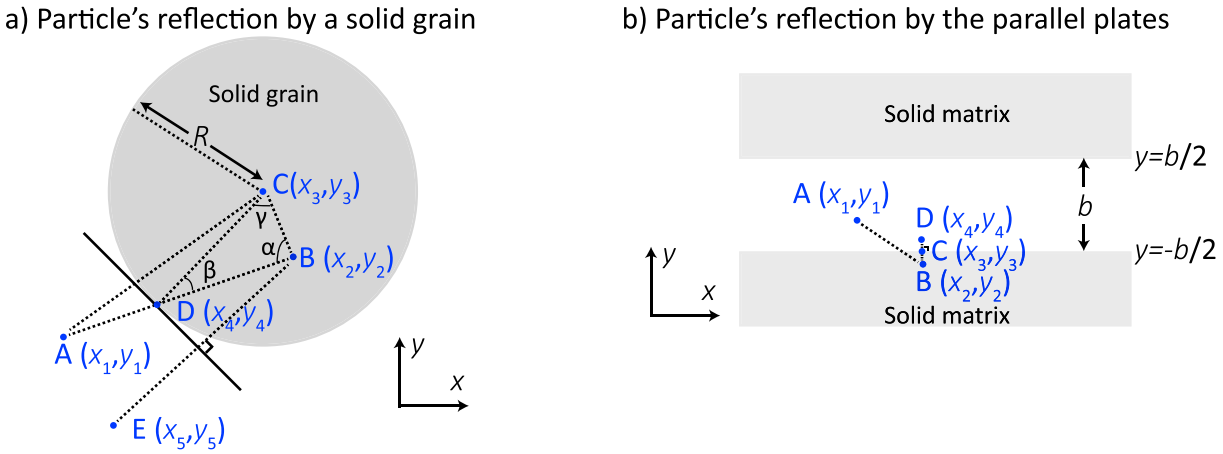

Figure 3. Illustration of particle's reflection by the solid circle within a fluidic plate (a) and by the parallel plates (b). (a) The particle moves from point A to point E by hitting the solid grain with a radius *R*. The mathematical expression for determining point E is based on the locations of point B (determined by the advective and diffusive jumps), point C (the center of solid grain), and point D (the intersection point). (b) The particle moves from point A to point D by hitting the bottom plate. The location of point D can be determined by the preknown points B and C. The details of mathematical derivations can be found in Appendix A.

The optimization algorithm for inversely estimating the mean velocity and D_L was conducted in MatLab to achieve the global minimum fitting errors. In total, we run 64 inversions for porous media cases and run 156 inversions for fracture cases.

3. Results and Discussions

3.1. The Oscillating Flow Field and Fluid Flux

The seismic wave (green line in Figure 4) with varying degrees of A and T led to the oscillating flow field in porous and fractured media. This has been demonstrated in porous media (Figure 4a when $\rho A/\nabla P = 1.4$ and $T = \tau$) and fracture (Figure 4b when $\rho A/\nabla P = 2$ and $T = \tau$). In these two specific cases when $T = \tau$ (Figure 4), the oscillating body force induced by the seismic wave led to the flow velocity acceleration and deceleration accordingly, that is, flow velocity field followed the same trend of the oscillating seismic wave. Specifically, the velocity field was accelerated compared to the steady flow case when time $< \tau/2$, since the seismic body force acted in the same direction as the steady flow. While the velocity field was decelerated when $\tau/2 <$ time $< \tau$, the imposed seismic force acted in the opposite direction to the steady flow. Consequently, the magnitude of velocity simultaneously reached its maximum (time $= \tau/4$) and minimum (time $= 3\tau/4$) when the seismic force increased up to its maxima and decreased down to its minima, respectively (Figure 4). Depending on the magnitude of $\rho A/\nabla P$, the minimum velocity can be negative if $\rho A/\nabla P > 1$, indicating the reverse flow might occur periodically (Figure 4b). In our simulations, the reverse flow occurred when using the wide range of $\rho A/\nabla P$ ($\rho A/\nabla P$ ranged from 0.2 to 1.6 for porous media, and it ranged from 0.5 to 10 for fractures).

An alternative way to diagnose the oscillating flow field was to integrate flux at the outbound; this yielded discharge Q. The oscillating feature of Q (the blue lines in Figure 4) strictly followed the trend of the seismic wave (e.g., the green lines in Figure 4); this is essentially because the acceleration or deceleration of the velocity field simultaneously followed the increased or decreased seismic force, respectively. The highest Q corresponded to the velocity field reaching its maxima, and vice versa. The oscillating feature of the velocity field in terms of magnitude and flow direction exerted a critical impact on the solute transport process as discussed below.

3.2. The Effects of Oscillating Flow Field on the BTCs

BTCs are the results of collective factors, including characteristics of the flow field (Le Borgne et al., 2008), types of solute source (point, line, and area) (Webster et al., 2007), boundary conditions (Dejam et al., 2014), and duration of transport process (i.e., length of domain, Wang et al., 2012). In this study, we focused on the effects of the oscillating flow field by eliminating other factors; this was achieved by using a flux weighted line source and no flux boundaries. Moreover, the fluidic plate and parallel plates were created long

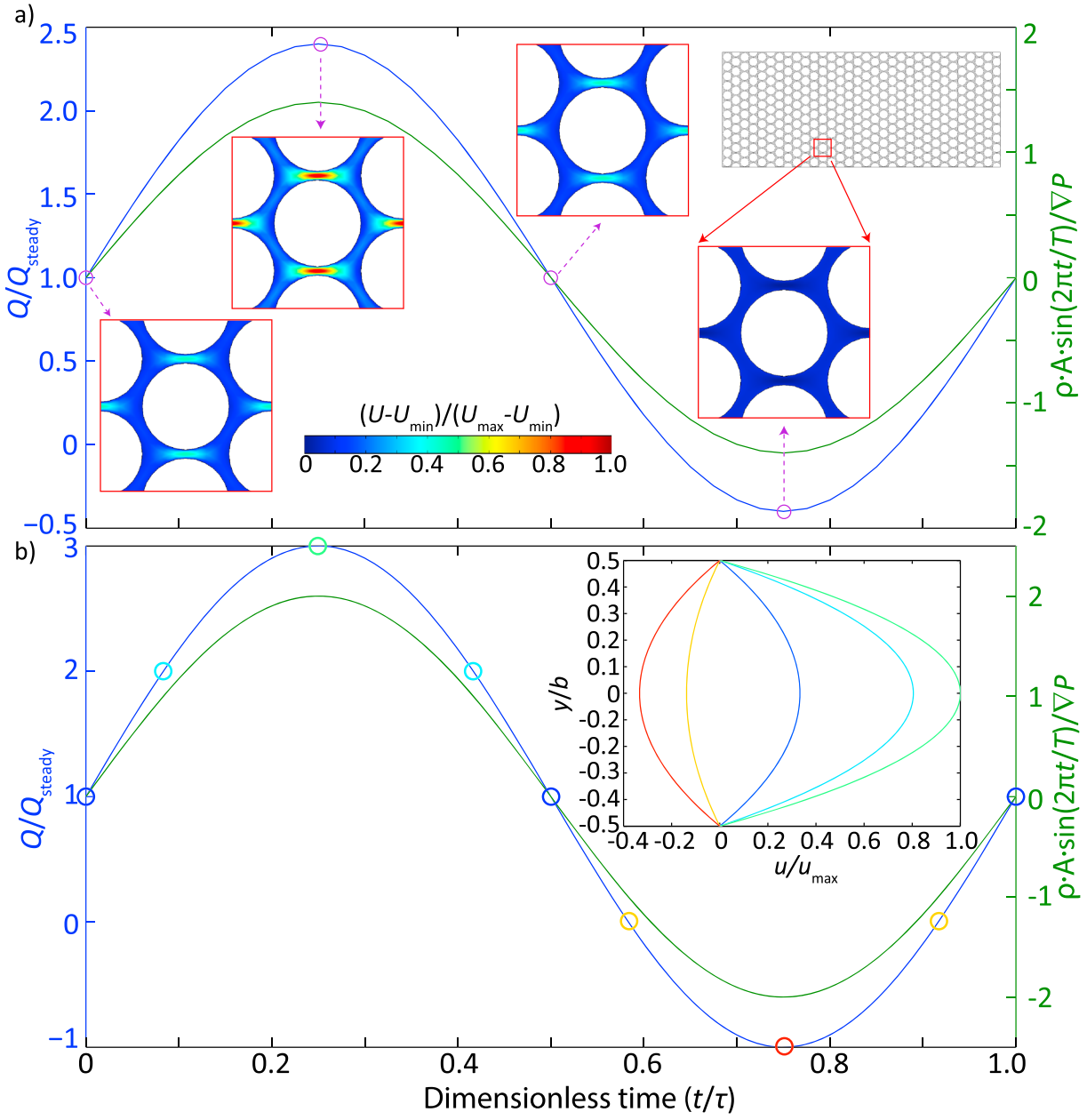

Figure 4. The schematic diagrams of the oscillating discharge Q (blue lines) and the oscillating velocity field for the fluidic plate (a) and the parallel plates (b). The oscillating flow field is subjected to a seismic wave (green lines) with amplitude A and period T, where Q_{steady} corresponds to the steady discharge without imposing the seismic force, τ is the pore volume (i.e., volume/discharge) of the fluidic plate or the parallel plates, ρ is the fluid density, t is the time, sin() represents the sinusoidal function, and ∇P is the pressure gradient. In these two cases, the flow field *resonates* with the finite porous and fractured media, that is, $T = \tau$. The insets in Figure 4a show the snapshots of the velocity field over time, where U is velocity magnitude with its maximum U_{max} and minimum U_{min}. The inset in Figure 4b shows the colored velocity profiles corresponding the velocity field over time as indicated by the same colored circles.

enough with the given ∇P to ensure asymptotic dispersion when the flow field was steady. This was demonstrated by the perfect fitting using the ADE for the BTC with $T = 0$, that is, the black dots in Figure 5. Thus, the preasymptotic dispersion regime was excluded in this study (Bolster et al., 2014) for the steady flow.

BTCs fairly showed Fickian transport when T was much larger ($T/\tau > 3$) or smaller ($T/\tau < 0.1$) than τ as demonstrated by the representative BTCs in the fluidic plate (Figure 5b). This observation also held true for transport in fractures (results are not shown here). The mean velocity in porous domain almost maintained unchanged for small T, but it increased when T became large (Figure 5a), which was also

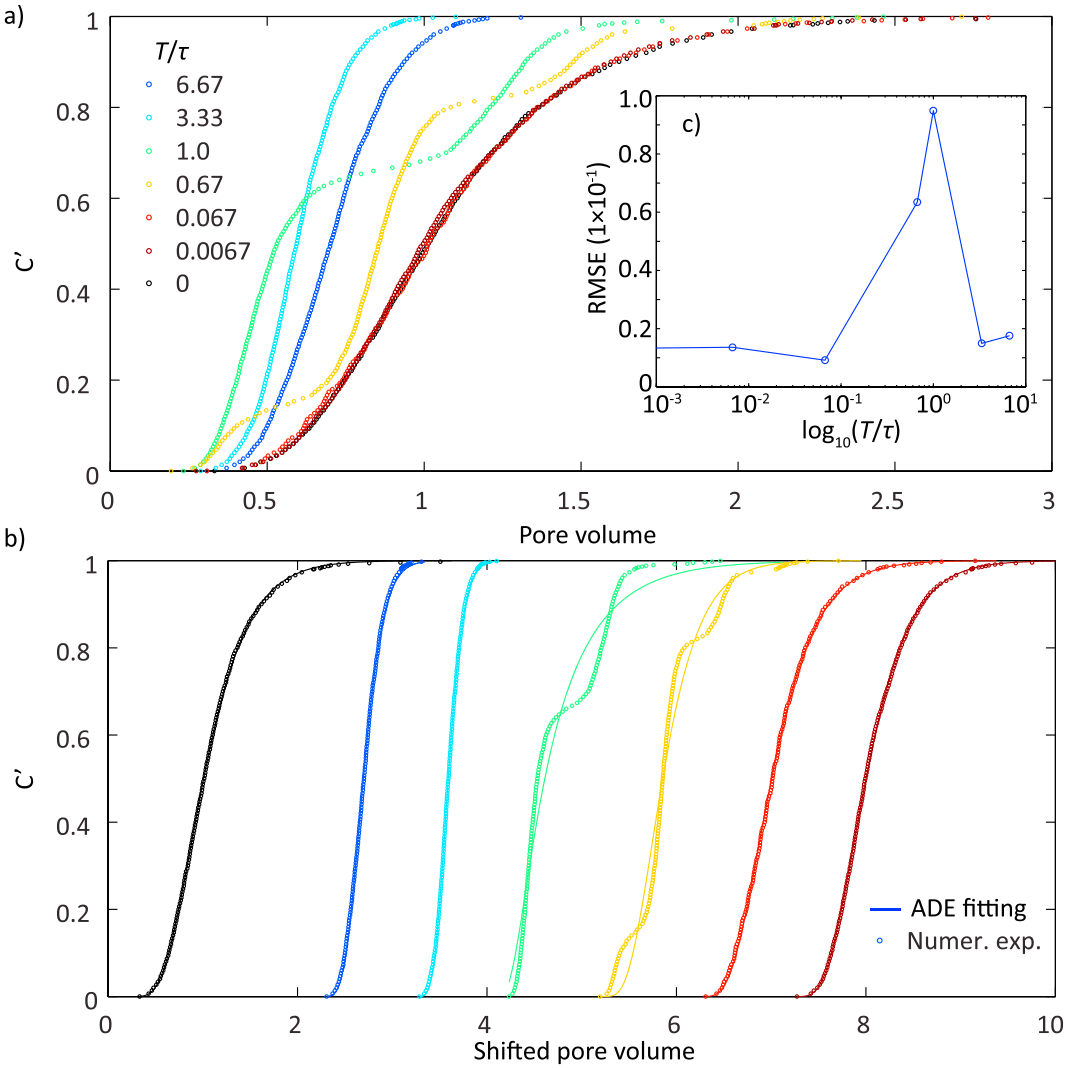

Figure 5. (a) The exemplary breakthrough curves from numerical experiments in the fluidic plate for cases with different period (T) but a constant amplitude of the seismic wave, where τ is the pore volume = volume/discharge. (b) The goodness of fitting the advection-dispersion equation (ADE) as denoted by lines to the numerically simulated breakthrough curves as shown by circles. Different color in Figure 5b corresponds to the seismic wave with different T in Figure 5a, but the x axis is shifted by one pore volume for each breakthrough curve. (c) The relationship between the root-mean-square error (RMSE) and T/τ, where the x axis is plotted at a logarithmic scale. The RMSE denotes the mean value of concentration difference between the analytical solutions to the ADE and the numerical results from implementing the particle tracking random walk.

suggested by the advance of plume in Figures 6 and 7 and in Movies S1–S8 in the supporting information. This is because the small T represents a seismic wave having a large f, where the very frequent perturbation of the velocity field does not contribute to altering D_L and the mean velocity (Figure 5a and $T/\tau < 1$ in Figures 6 and 7) due to the short response time (Beresnev, 2006). The above statement is consistent with many previous studies that focused on infinite domain (Dreuzy et al., 2012) where τ is infinite large and T is comparably tiny. On the other hand, the large T represents a seismic wave with a small f, where the effects of slow perturbation were not prominent on altering dispersion, since solute breakthroughed the domain much faster than the perturbation effect manifested (Figure 5b and $T/\tau > 1$ in Figures 6 and 7). Moreover, the mean velocity was accelerated when T was large (Figures 5–7 and Movies S2 and S6 in the supporting information), because the seismic force that was initially applied aligned with the steady flow direction in this study (Figure 2). Likewise, the mean velocity would be presumably decelerated if the seismic force was initially imposed in the direction opposite to the steady flow. Therefore, the mean velocity depends on the direction of the seismic force when the seismic wave penetrates to the finite domain.

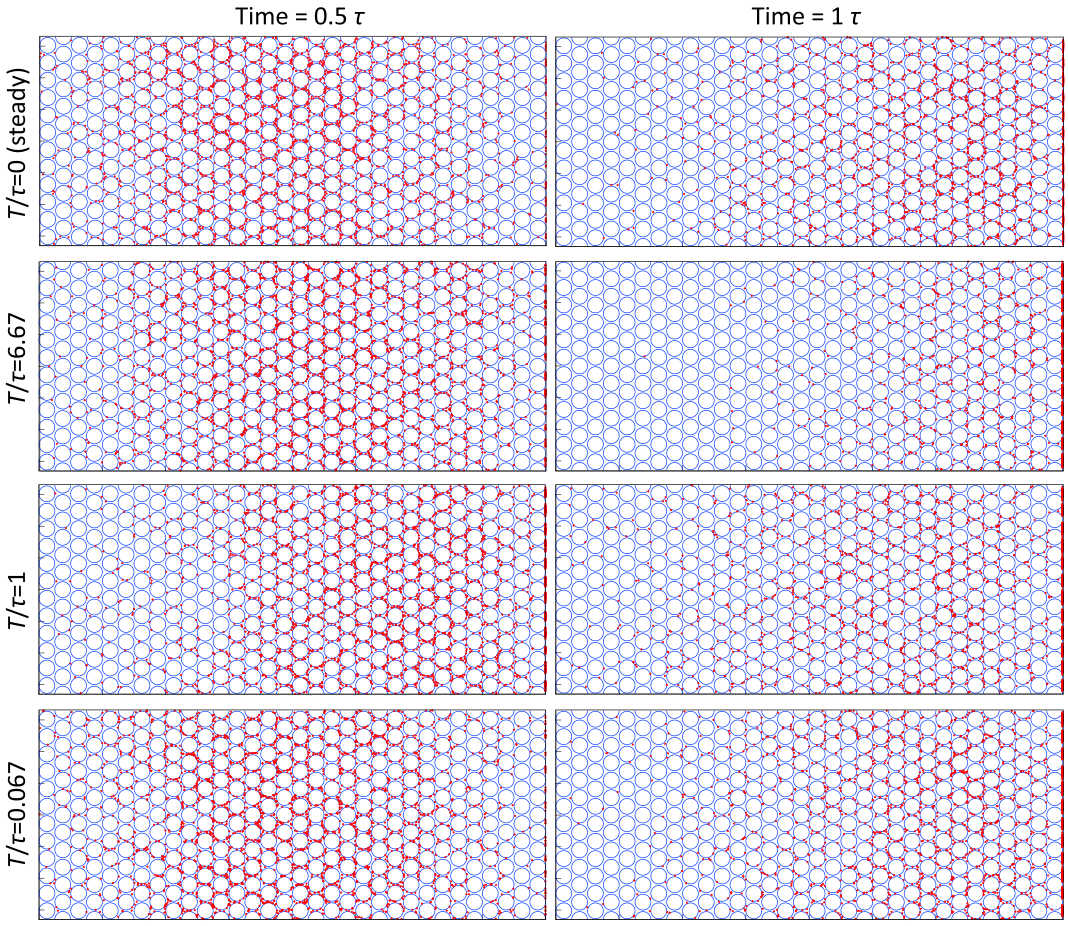

Figure 6. The snapshots of particle transport through the fluidic plate at time = 0.5 pore volume (the left panel) and time = 1 pore volume (the right panel), where the pore volume (τ) = volume/discharge = 151.3 s. Four cases are demonstrated here when the flow field is steady (in the first row), and when the flow field is oscillating (from the second to the fourth rows) induced by the seismic waves with a constant dimensionless amplitude $\rho A/\nabla P = 0.8$ but different dimensionless period T/τ (T/τ = 6.67, 1.0, and 0.067 for the second to the fourth rows). ρ is fluid density, ∇P is pressure gradient, A represents the acceleration amplitude of the seismic force $F = -\rho A \sin(2\pi ft)$, f is frequency (i.e., the reciprocal of period T) of the seismic wave, t is time, and sin() represents the sinusoidal function.

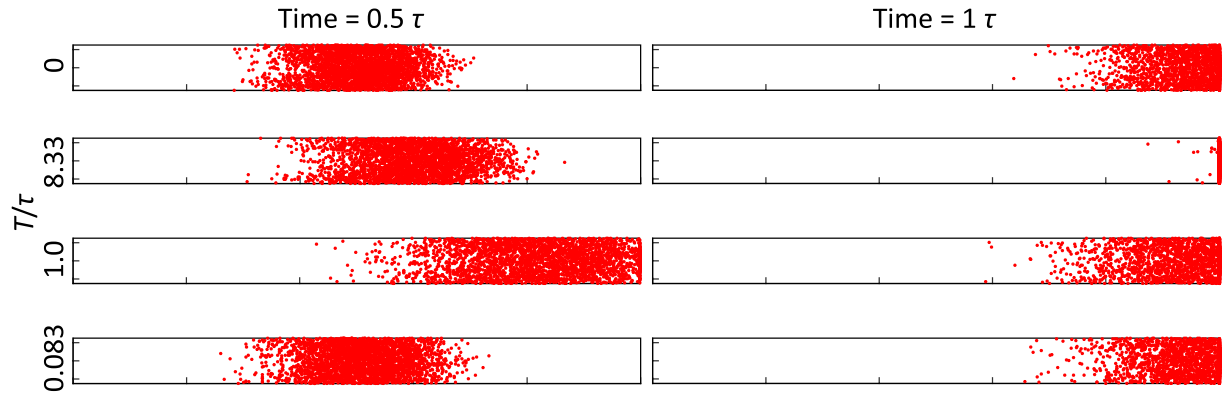

Figure 7. The snapshots of particle transport through the parallel plates at time = 0.5 pore volume (the left panel) and time = 1 pore volume (the right panel), where the pore volume (τ) = volume/discharge = 120 s. Four cases are demonstrated here when the flow field is steady ($T/\tau = 0$ in the first row), and when the flow field is oscillating (from the second to the fourth rows) induced by the seismic waves with a constant dimensionless amplitude $\rho A/\nabla P = 1$ but different dimensionless period T/τ (T/τ = 8.33, 1.0, and 0.083 for the second to the fourth rows). ρ is fluid density, ∇P is pressure gradient, A represents the acceleration amplitude of the seismic force $F = -\rho A \sin(2\pi ft)$, f is frequency (i.e., the reciprocal of period T) of the seismic wave, t is time, and sin() represents the sinusoidal function.

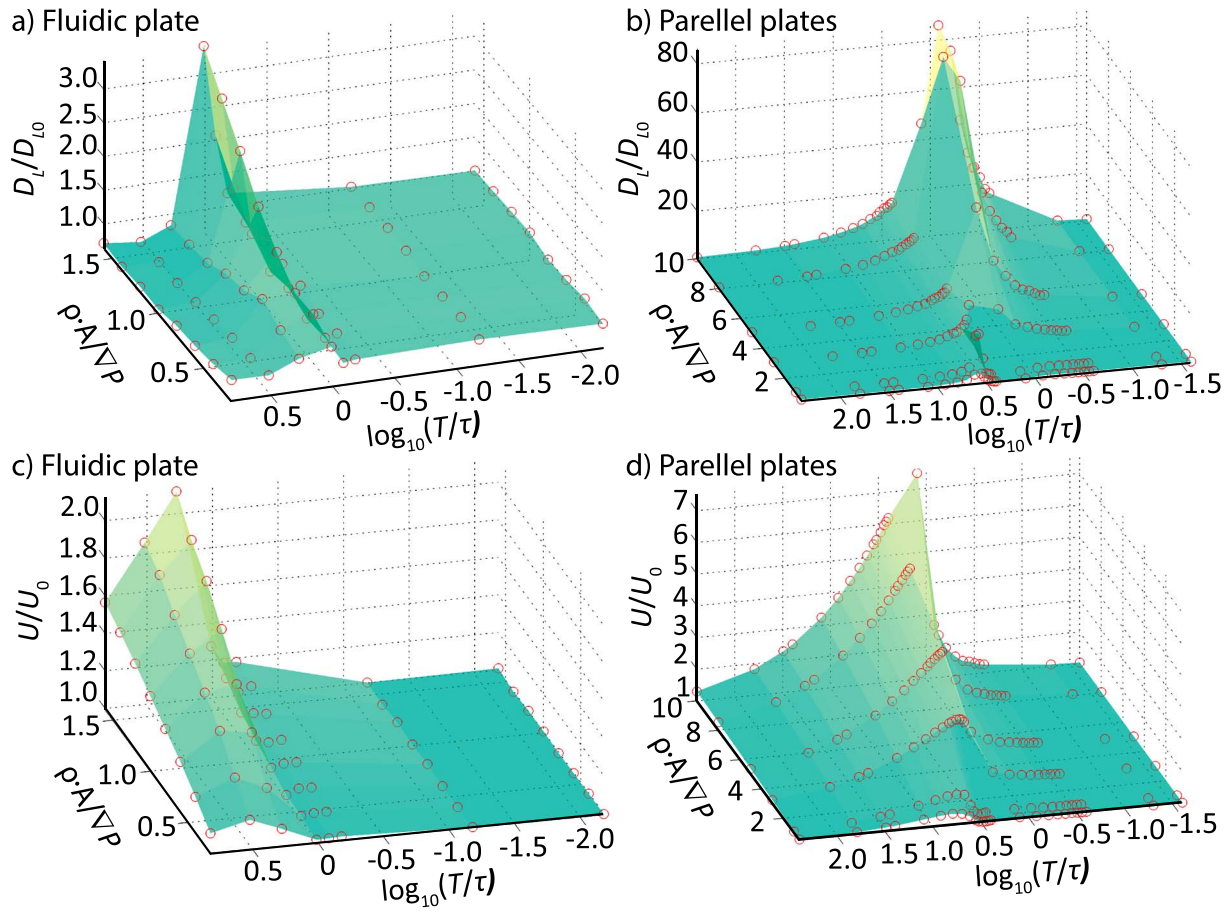

Figure 8. The relationships of the longitudinal dispersion coefficient (D_L) (a and b) and the mean velocity (U) (c-d) with the dimensionless period (T/τ) and dimensionless amplitude ($\rho A/\nabla P$) of the seismic wave within the fluidic plate and the parallel plates, where τ is the pore volume = volume/discharge, D_L and U are estimated by fitting the advection-dispersion equation to the experimental breakthrough curves; D_{L0} and U_0 are the counterparts corresponding to the steady flow field without applying the seismic force, ρ is fluid density, ∇P is pressure gradient, A represents the acceleration amplitude of the seismic force $F = -\rho A \sin(2\pi f t)$, f is frequency (i.e., the reciprocal of period T) of the seismic wave, t is time, and sin() represents the sinusoidal function.

More interestingly, BTCs showed non-Fickian behavior with early arrival and heavy tailing when the fluctuating flow field resonates with the finite system (green and yellow curves in Figure 5, $T/\tau = 1$ in Figures 6 and 7, and Movies S3 and S7 in the supporting information), that is, T is close to τ. This led to the broadest BTCs spanning almost 2.5 pore volumes when $T/\tau = 1$ (Figure 5a), which also corresponded to the broadest spreading of solutes when $T/\tau = 1$ compared to the cases with T/τ being further apart from 1 (Movies S1–S8 in the supporting information). Essentially, solute was accelerated first leading to fast arrival, and it was decelerated afterward where the reverse flow might occur, which led to a long tailing feature in the BTCs (Figure 5a and $T/\tau = 1$ in Figures 6 and 7). Therefore, the closer T is to τ, the larger degree of non-Fickian transport manifests. The degree of non-Fickian transport was demonstrated by the root-mean-square error when fitting the advection-dispersion equation to the numerically-derived BTCs (Figure 5c).

It should be noted that the above-mentioned arguments are valid when the amplitude of the seismic force (i.e., ρA) is not negligible compared to ∇P; this is demonstrated by Figures 5–7 where $\rho A/\nabla P > 0.8$. When ∇P dominates over the seismic forces (i.e., $\rho A/\nabla P << 1$), this leads to a negligible effect of the oscillating velocity field on the mean velocity and D_L (Figure 8).

3.3. Pore-Scale Perspective of Seismicity-Affected Macrodispersion

We obtained 64 and 128 sets of the mean velocity and D_L for the fluidic plate and for the parallel plates, respectively, considering a broad range of $\rho A/\nabla P$ and T/τ. The mean velocity and D_L were estimated by

fitting the advection-dispersion equation to the numerically-derived BTCs; both of them were further connected to $\rho A/\nabla P$ and T/τ for the fluidic plate and for the parallel plates (Figure 8).

3.3.1. Effects of the Oscillating Flow Field on the Apparent Macrodispersion Coefficient

Generally speaking, with increasing T/τ for a given $\rho A/\nabla P$, D_L reached its maxima when T/τ approached 1 (i.e., $\log_{10}(T/\tau) \approx 0$ at the logarithmic scale) and afterward decreased to its counterpart (D_{L0}) that was estimated for the steady flow field (i.e., $A = 0$, Figures 8a and 8b). Hereafter, the maximum D_L is called as the resonant D_L when $T/\tau \approx 1$. The trend of D_L with increasing T/τ is consistent with the transition of transport regime. That is, as T/τ increased, transport gradually transitioned from Fickian to non-Fickian regimes (Figure 5) when the oscillating flow field resonates with the finite porous and fractured systems (i.e., $T/\tau = 1$), while a further increase in T/τ (>1) would induce transport to transition back to Fickian regime (Figure 5). All these transitions are fundamentally attributed to a fact that the oscillating flow field and consequently the solute transport process resonates with the finite pore-scale system when T approaches τ, where the fast arrival and heavy tailing in the BTCs is expected to occur (Figure 5 and $T/\tau = 1$ in Figures 6 and 7).

Moreover, the degree of enhancement for the resonant D_L strictly depends on the amplitude of velocity fluctuations (i.e., $\rho A/\nabla P$). The resonant D_L increases exponentially with $\rho A/\nabla P$ at different increasing rates for the fluidic plate and for the parallel plates (Figures 8a and 8b). For example, the maximum $\rho A/\nabla P$ are 1.6 and 10 for the fluidic plate and for the parallel plates, respectively, but the maximum D_L/D_{L0} are 3.4 and 82.3, respectively. The difference of the increase in D_L suggests that, in addition to the effect of $\rho A/\nabla P$, the enhancement of resonant D_L is tightly dependent on the geometry and the pattern of flow field (Cirpka et al., 2015; Wang & Cardenas, 2017).

Aside from increasing D_L when the flow field resonates with the finite systems (Figures 5 and 8), our study demonstrates that D_L could be slightly reduced (i.e., $D_L/D_{L0} < 1$) when $T/\tau > 1$ (Figures 8a and 8b). The reduction in D_L occurred, because solute breakthroughed the domain much earlier than the time for flushing the entire system (see $T/\tau > 1$ in Figures 6 and 7). That is, the earlier breakthrough with a fast mean velocity slightly lessened the degree of solute spreading, which is different from the conventional view: the dispersion coefficient is proportional to the mean velocity (Bear, 1972).

3.3.2. Effects of the Oscillating Flow Field on the Mean Velocity

In addition to the effects on D_L, the oscillating flow field can significantly alter the mean velocity in a finite domain when $T/\tau > 1$, but it plays a trivial role in changing the mean velocity when $T/\tau < 1$ (Figures 8c and 8d). In our study, the onset of the seismic force was applied in the same direction as the steady flow field (Figure 2); therefore, the mean velocity was enhanced to some extent (Figures 8c and 8d). The degree of velocity enhancement (U/U_0) depended on the magnitude of $\rho A/\nabla P$ and T/τ., where U is the mean velocity for the oscillating flow field, and U_0 is the counterpart for a steady flow field.

Similar to the trend of D_L with increasing T/τ, for a given $\rho A/\nabla P$, U/U_0 increased at first and then asymptotically decreased with T/τ (Figures 8c and 8d). However, U/U_0 reached its maxima at $\log_{10}(T/\tau) \approx 0.5$, while D_L/D_{L0} reached its maxima when $\log_{10}(T/\tau) = 0$. This is because U is greatly enhanced when the oscillating flow field is experiencing the positive seismic force (time/$\tau < 0.25$ in Figure 2), that is, the seismic force aligns with the direction of the steady flow. Any system that has a T/τ that is further away from the threshold, that is, $\log_{10}(T/\tau) = 0.5$, the effects of positive and negative seismic forces would to some extent cancel each other out, or the effects of seismic forces gradually diminish; this eventually resulted in a relatively small U (Figures 8c and 8d).

Moreover, for a given T/τ and when $T/\tau > 1$, U/U_0 increases monotonically with $\rho A/\nabla P$, this is due to a fact that the larger $\rho A/\nabla P$ is, the greater degree of oscillation (Figure 2), where the positive and negative contributions induced by seismicity were not fully canceled out since $T/\tau > 1$.

4. Implications of the Effects of the Oscillating Flow in a Finite Domain

Many geophysical mysteries are underpinned by the flow and transport processes (Alley et al., 2002). While extensive researches have focused on the steady flow and associated transport processes (Le Borgne et al., 2008), how the transient flow fields, especially the oscillating flow features, in a

finite domain affect transport process remains unclear. Based on pore-scale simulations, our study reveals the underpinning physics by quantitatively relating the mean velocity and the apparent macrodispersion coefficient to the frequency and amplitude of the seismicity-induced oscillating flow field.

The results from two-hundred twenty simulations for the fluidic plate and parallel plates suggested that the effects of the oscillating flow field were trivial on altering U and D_L when T was much less than τ for a finite system. That is, the fast oscillating flow field only added white noise to the BTCs, where the transport regime remained unchanged compared to the corresponding cases with a steady flow field. On the other hand, the effects of the oscillating flow field on U and D_L became remarkable when T was close to τ, where the degree of enhancement of U and D_L depended on $\rho A/\nabla P$.

Although the oscillating flow fields were only generated by applying the seismic forces with a varying degree of A and T, the oscillating flow features induced by other factors (e.g., fluctuating boundary conditions) can be well preserved and reproduced by introducing the seismic wave. For example, the seasonally and daily fluctuating river water level drives the oscillating hyporheic flux (Boutt & Fleming, 2009) and the fluctuating tides that affect the oscillating submarine groundwater discharge (Sawyer et al., 2013). Note that all these above-mentioned natural systems have a finite domain subjected to an oscillating flow field. Our results can be broadly applied to better predict the fate and transport of dissolved substances considering oscillating flow fields and thus might shed light on, for example, the sustainability and vulnerability of groundwater system along the coastal lines (Sawyer et al., 2016).

5. Conclusions

To address the underpinning mechanisms of how the oscillating flow field affects macrodispersion, we conducted two-hundred twenty pore-scale numerical experiments for examining the transport process through the idealized finite porous and fractured domains. The oscillating flow field was induced by imposing a seismic force that followed a sinusoidal function with a varying degree of amplitude and frequency. We fitted the advection-dispersion equation to the resultant BTCs to obtain the mean velocity and apparent dispersion coefficient (D_L). Our pore-scale study focusing on the finite domains quantitatively showed the resonant features of the transport process. This is demonstrated by a fact that D_L reached its maxima when the period (T) of the oscillating flow field approximated the pore volume τ (= volume/discharge) of a finite system, that is, the oscillating flow field resonates with the finite system. The degree of enhancement of dispersion diminished when T was further apart from τ. Moreover, when $T/\tau = 1$, D_L increased exponentially with the amplitude of the seismic force. The mean velocity was also enhanced to some extent when $T > \tau$, because the imposed seismic force was initially applied in the same direction as the pressure-driven flow. The information of the mean velocity and D_L considering the seismicity effects can be used to predict the fate and transport of solute in many geological settings via the classical advection-dispersion equation.

Appendix A

A1. Particles' Reflection by a Circle Grain

Assuming that a particle, located at its current position A (x_1, y_1), has a jumping distance due to advection and diffusion that might penetrate into the solid grain at the position B (x_2, y_2; Figure 3a), the associated reflection location outside of the circle grain is E (x_5, y_5) considering no energy loss during the physical rebounding steps from A to D and to E (Figure 3a).

In this case, the spatial locations of points A–C are known as a priori. The calculations for estimating the relevant angles (α, β, and γ) are based on the locations of points A–C and the radius (R) of solid grain. This is demonstrated by equations (A1)–(A3). The information of the relevant angles and the points' locations (A–C) is further used to determine the point D (x_4, y_4) and eventually the targeted point E (x_5, y_5).

$$\alpha = \arccos\left(\frac{(x_3-x_2)(x_1-x_2)+(y_3-y_2)(y_1-y_2)}{\sqrt{(x_3-x_2)^2+(y_3-y_2)^2}\sqrt{(x_1-x_2)^2+(y_1-y_2)^2}}\right) \tag{A1}$$

$$\beta = \arcsin\left(\sqrt{(x_3-x_2)^2+(y_3-y_2)^2}\,\frac{\sin(\alpha)}{R}\right) \tag{A2}$$

$$\gamma = \pi-\alpha-\beta \tag{A3}$$

$$(x_4,y_4) = \left(x_2-\frac{(x_2-x_1)}{\sqrt{(x_2-x_1)^2+(y_2-y_1)^2}}\frac{\sin(\gamma)R}{\sin(\alpha)}, y_2-\frac{(y_2-y_1)}{\sqrt{(x_2-x_1)^2+(y_2-y_1)^2}}\frac{\sin(\gamma)R}{\sin(\alpha)}\right) \tag{A4}$$

$$(x_5,y_5) = \left(x_2-2(x_3-x_4)\frac{(x_3-x_4)x_2+(y_3-y_4)y_2+(x_4-x_3)x_4+(y_4-y_3)y_4}{(x_3-x_4)^2+(y_3-y_4)^2}, y_2 \right. \tag{A5}$$
$$\left. -2(y_3-y_4)\frac{(x_3-x_4)x_2+(y_3-y_4)y_2+(x_4-x_3)x_4+(y_4-y_3)y_4}{(x_3-x_4)^2+(y_3-y_4)^2}\right)$$

A2. Particles' Reflection by the Parallel Plates

Assuming that a particle, located at its current position A (x_1, y_1), has a jumping distance due to advection and diffusion that might penetrate into the parallel plates (with a distance b between the top and bottom surfaces) at the position B (x_2, y_2), the associated reflection location within the parallel plates is point D (x_4, y_4) considering no energy loss during the physical rebounding steps from A to C and to D (Figure 3b).

In this case, the spatial locations of points A–C are known as a priori. The reflection point D (x_4, y_4) can be simply quantified by equation (A6).

$$(x_4,y_4) = (x_2,-b-y_2) \tag{A6}$$

Acknowledgments
This work is supported by the Geology Foundation of the University of Texas. Additional financial support is provided by the Tianjin University. All simulation results are presented in Figures and Movies in the supplementary information. We thank the reviewer Chiyu Xie for the insightful comments to improve our paper. We also thank Editor Douglas Schmitt for handling this paper.

References

Alley, W. M., Healy, R. W., LaBaugh, J. W., & Reilly, T. E. (2002). Flow and storage in groundwater systems. *Science*, *296*(5575), 1985–1990. https://doi.org/10.1126/science.1067123

Bear, J. (1972). *Dynamics of fluids in porous media*. New York: American Elsevier Pub. Co.

Befus, K. M., Cardenas, M. B., Erler, D. V., Santos, I. R., & Eyre, B. D. (2013). Heat transport dynamics at a sandy intertidal zone. *Water Resources Research*, *49*, 3770–3786. https://doi.org/10.1002/wrcr.20325

Beresnev, I. A. (2006). Theory of vibratory mobilization on nonwetting fluids entrapped in pore constrictions. *Geophysics*, *71*(6), N47–N56. https://doi.org/10.1190/1.2353803

Bolster, D., Méheust, Y., Le Borgne, T., Bouquain, J., & Davy, P. (2014). Modeling preasymptotic transport in flows with significant inertial and trapping effects—The importance of velocity correlations and a spatial Markov model. *Advances in Water Resources*, *70*(0), 89–103. https://doi.org/10.1016/j.advwatres.2014.04.014

Boutt, D. F., & Fleming, B. J. (2009). Implications of anthropogenic river stage fluctuations on mass transport in a valley fill aquifer. *Water Resources Research*, *45*, W09546. https://doi.org/10.1029/2007WR006526

Chambers, D. P., Mehlhaff, C. A., Urban, T. J., & Nerem, R. S. (2002). Analysis of interannual and low-frequency variability in global mean sea level from altimetry and tide gauges. *Physics and Chemistry of the Earth, Parts A/B/C*, *27*(32-34), 1407–1411. https://doi.org/10.1016/S1474-7065(02)00078-5

Chatwin, P. (1975). On the longitudinal dispersion of passive contaminant in oscillatory flows in tubes. *Journal of Fluid Mechanics*, *71*(03), 513–527. https://doi.org/10.1017/S0022112075002716

Cirpka, O. A., & Attinger, S. (2003). Effective dispersion in heterogeneous media under random transient flow conditions. *Water Resources Research*, *39*(9), 1257. https://doi.org/10.1029/2002WR001931

Cirpka, O. A., Chiogna, G., Rolle, M., & Bellin, A. (2015). Transverse mixing in three-dimensional nonstationary anisotropic heterogeneous porous media. *Water Resources Research*, *51*, 241–260. https://doi.org/10.1002/2014WR015331

Dejam, M., Hassanzadeh, H., & Chen, Z. (2014). Shear dispersion in a fracture with porous walls. *Advances in Water Resources*, *74*, 14–25. https://doi.org/10.1016/j.advwatres.2014.08.005

Deng, W., & Cardenas, M. B. (2013). Dynamics and dislodgment from pore constrictions of a trapped nonwetting droplet stimulated by seismic waves. *Water Resources Research*, *49*, 4206–4218. https://doi.org/10.1002/wrcr.20335

Dentz, M., & Carrera, J. (2003). Effective dispersion in temporally fluctuating flow through a heterogeneous medium. *Physical Review E*, *68*(3), 036310. https://doi.org/10.1103/Physreve.68.036310

Dentz, M., & Carrera, J. (2005). Effective solute transport in temporally fluctuating flow through heterogeneous media. *Water Resources Research*, *41*, W00D10. https://doi.org/10.1029/2004WR003571

Dentz, M., Carrera, J., & De Dreuzy, J.-R. (2011). Erratum: Effective dispersion in temporally fluctuating flow through a heterogeneous medium. *Physical Review E*, *84*(1), 019904. https://doi.org/10.1103/PhysRevE.84.019904

Dentz, M., le Borgne, T., Englert, A., & Bijeljic, B. (2011). Mixing, spreading and reaction in heterogeneous media: A brief review. *Journal of Contaminant Hydrology*, *120*, 1–17. https://doi.org/10.1016/j.jconhyd.2010.05.002

Deon, K., H, S. A., T, B. R., T, M. C., & Samuel, B. (2017). Tidal controls on riverbed denitrification along a tidal freshwater zone. *Water Resources Research*, *53*, 799–816. https://doi.org/10.1002/2016WR019405

Detwiler, R. L., Rajaram, H., & Glass, R. J. (2002). Experimental and simulated solute transport in a partially-saturated, variable-aperture fracture. *Geophysical Research Letters*, *29*(8), W10410. https://doi.org/10.1029/2001GL013508

Dreuzy, J. R., Carrera, J., Dentz, M., & Borgne, T. L. (2012). Asymptotic dispersion for two-dimensional highly heterogeneous permeability fields under temporally fluctuating flow. *Water Resources Research*, *48*, W01532. https://doi.org/10.1029/2011WR011129

Elfeki, A. M., Uffink, G. J., & Lebreton, S. (2007). Simulation of solute transport under oscillating groundwater flow in homogeneous aquifers. *Journal of Hydraulic Research*, *45*(2), 254–260. https://doi.org/10.1080/00221686.2007.9521760

Elsworth, D., Spiers, C. J., & Niemeijer, A. R. (2016). Understanding induced seismicity. *Science*, *354*(6318), 1380–1381. https://doi.org/10.1126/science.aal2584

Fischer, H. B., List, E. J., Koh, R. C. Y., Imberger, J., & Brooks, N. H. (1979). *Mixing in inland and coastal waters*. San Diego, Calif: Academic.

Gelhar, L. W., & Axness, C. L. (1983). Three-dimensional stochastic analysis of macrodispersion in aquifers. *Water Resources Research*, *19*(1), 161–180. https://doi.org/10.1029/WR019i001p00161

Gelhar, L. W., Welty, C., & Rehfeldt, K. R. (1992). A critical review of data on field-scale dispersion in aquifers. *Water Resources Research*, *28*(7), 1955–1974. https://doi.org/10.1029/92WR00607

Ito, Y., & Obara, K. (2006). Very low frequency earthquakes within accretionary prisms are very low stress-drop earthquakes. *Geophysical Research Letters*, *33*, L09302. https://doi.org/10.1029/2006GL025883

James, S. C., Bilezikjian, T., & Chrysikopoulos, C. (2005). Contaminant transport in a fracture with spatially variable aperture in the presence of monodisperse and polydisperse colloids. *Stochastic Environmental Research and Risk Assessment*, *19*(4), 266–279. https://doi.org/10.1007/s00477-004-0231-3

James, S. C., & Chrysikopoulos, C. V. (2000). Transport of polydisperse colloids in a saturated fracture with spatially variable aperture. *Water Resources Research*, *36*(6), 1457–1465. https://doi.org/10.1029/2000WR900048

Kang, P. K., Brown, S., & Juanes, R. (2016). Emergence of anomalous transport in stressed rough fractures. *Earth and Planetary Science Letters*, *454*, 46–54. https://doi.org/10.1016/j.epsl.2016.08.033

Kiel, B. A., & Bayani Cardenas, M. (2014). Lateral hyporheic exchange throughout the Mississippi River network. *Nature Geoscience*, *7*(6), 413–417. https://doi.org/10.1038/ngeo2157

Le Borgne, T., Dentz, M., & Carrera, J. (2008). Spatial Markov processes for modeling Lagrangian particle dynamics in heterogeneous porous media. *Physical Review E*, *78*(2 Pt 2), 026308. https://doi.org/10.1103/PhysRevE.78.026308

Manga, M., Beresnev, I., Brodsky, E. E., Elkhoury, J. E., Elsworth, D., Ingebritsen, S. E., et al. (2012). Changes in permeability caused by transient stresses: Field observations, experiments, and mechanisms. *Reviews of Geophysics*, *50*, RG2004. https://doi.org/10.1029/2011RG000382

Michael, B., Douglas, A., Eric, K., Paulo, F. L., Bruce, F., Robert, S., & Janet, B. (2005). Seasonal fluctuations in the mass of the Amazon River system and Earth's elastic response. *Geophysical Research Letters*, *32*, L16308. https://doi.org/10.1029/2005GL023491

Pool, M., Dentz, M., & Post, V. E. A. (2016). Transient forcing effects on mixing of two fluids for a stable stratification. *Water Resources Research*, *52*, 7178–7197. https://doi.org/10.1002/2016WR019181

Pride, S. R., Berryman, J. G., & Harris, J. M. (2004). Seismic attenuation due to wave-induced flow. *Journal of Geophysical Research*, *109*, B01201. https://doi.org/10.1029/2003JB002639

Rehfeldt, K. R., & Gelhar, L. W. (1992). Stochastic-analysis of dispersion in unsteady-flow in heterogeneous aquifers. *Water Resources Research*, *28*(8), 2085–2099. https://doi.org/10.1029/92WR00750

Sawyer, A. H., David, C. H., & Famiglietti, J. S. (2016). Continental patterns of submarine groundwater discharge reveal coastal vulnerabilities. *Science*, *353*(6300), 705–707. https://doi.org/10.1126/science.aag1058

Sawyer, A. H., Shi, F., Kirby, J. T., & Michael, M. A. (2013). Dynamic response of surface water-groundwater exchange to currents, tides, and waves in a shallow estuary. *Journal of Geophysical Research: Oceans*, *118*, 1749–1758. https://doi.org/10.1002/jgrc.20154

Wang, L., & Cardenas, M. B. (2014). Non-Fickian transport through two-dimensional rough fractures: Assessment and prediction. *Water Resources Research*, *50*, 871–884. https://doi.org/10.1002/2013WR014459

Wang, L., & Cardenas, M. B. (2015). An efficient quasi-3D particle tracking-based approach for transport through fractures with application to dynamic dispersion calculation. *Journal of Contaminant Hydrology*, *179*, 47–54. https://doi.org/10.1016/j.jconhyd.2015.05.007

Wang, L., & Cardenas, M. B. (2017). Transition from non-Fickian to Fickian longitudinal transport through 3-D rough fractures: Scale-(in) sensitivity and roughness dependence. *Journal of Contaminant Hydrology*, *198*, 1–10. https://doi.org/10.1016/j.jconhyd.2017.02.002

Wang, L., Cardenas, M. B., Deng, W., & Bennett, P. C. (2012). Theory for dynamic longitudinal dispersion in fractures and rivers with Poiseuille flow. *Geophysical Research Letters*, *39*, L05401. https://doi.org/10.1029/2011GL050831

Webster, D. R., Felton, D. S., & Luo, J. (2007). Effective macroscopic transport parameters between parallel plates with constant concentration boundaries. *Advances in Water Resources*, *30*(9), 1993–2001. https://doi.org/10.1016/j.advwatres.2007.04.004

Weingarten, M., Ge, S., Godt, J. W., Bekins, B. A., & Rubinstein, J. L. (2015). High-rate injection is associated with the increase in U.S. mid-continent seismicity. *Science*, *348*(6241), 1336–1340. https://doi.org/10.1126/science.aab1345

Zhang, D., & Neuman, S. P. (1996). Head and velocity covariances under quasi-steady state flow and their effects on advective transport. *Water Resources Research*, *32*(1), 77–83. https://doi.org/10.1029/95WR02766

Zhang, P., Devries, S. L., Dathe, A., & Bagtzoglou, A. C. (2009). Enhanced mixing and plume containment in porous media under time-dependent oscillatory flow. *Environmental science & technology*, *43*(16), 6283–6288. https://doi.org/10.1021/es900854r